Cell Biomaterials

Article

Desmoplastic tumor priming using clinical-stage corticosteroid liposomes

Graphical abstract

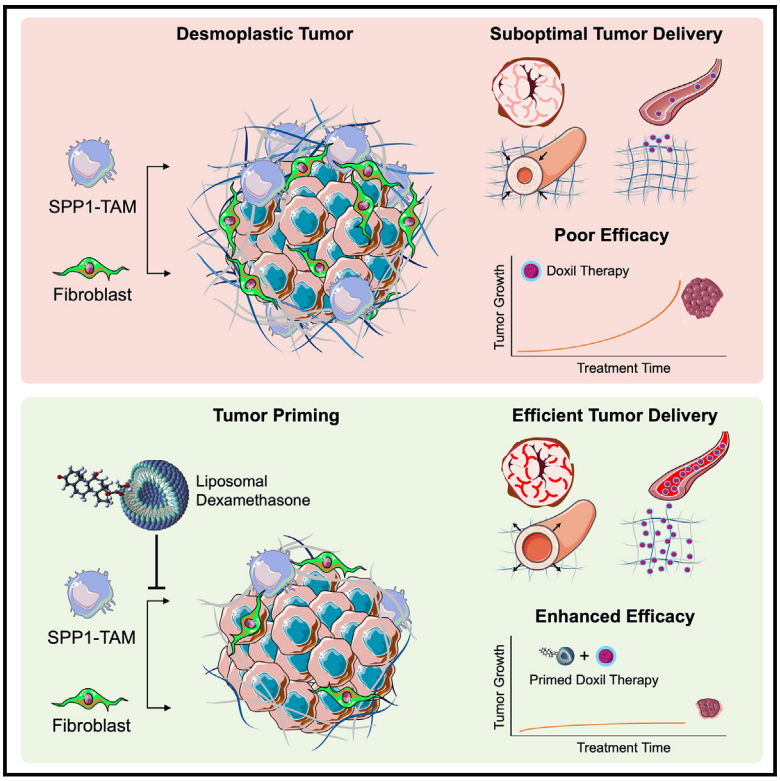

Highlights

- Liposomal dexamethasone depletes profibrotic SPP1^{+} tumor-associated macrophages
- Liposomal dexamethasone reduces tumor extracellular matrix deposition
- Tumor microenvironment priming with liposomal dexamethasone improves drug delivery
- Liposomal dexamethasone pre-treatment enhances the efficacy of cancer nanotherapy

Authors

Tarun Ojha, Gideon J.L. Schaefer, Rahaf Mihyar, ..., Gert Storm, Josbert Metselaar, Twan Lammers

Correspondence

tlammers@ukaachen.de

In brief

Tumor inflammation can create a hostile microenvironment that limits drug delivery. This study shows that clinical-stage liposomal dexamethasone can reprogram the tumor microenvironment, improving blood vessel perfusion and reducing extracellular matrix deposition. As a result of this, the accumulation, penetration, and distribution of subsequently administered drugs and drug delivery systems can be improved, resulting in improved antitumor treatment efficacy in desmoplastic cancers.

Ojha et al., 2025, Cell Biomaterials *1*, 100051
April 22, 2025
https://doi.org/10.1016/j.celbio.2025.100051

CellPress

Cell Biomaterials

CellPress
OPEN ACCESS

Article

Desmoplastic tumor priming using clinical-stage corticosteroid liposomes

Tarun Ojha,[1,2] Gideon J.L. Schaefer,[3] Rahaf Mihyar,[1] Vertika Pathak,[1] Josef Ehling,[1] Elena Rama,[1] Federica De Lorenzi,[1] Asmaa Said Elshafei,[1] Diana Moeckel,[1] Sara Elsafy,[1] Benjamin Theek,[1] Maike Wagner,[1] Paolo Ceccarini,[1] Lorena Consolino,[1] Marek Weiler,[1] Fabian Peisker,[3] Tim Caspers,[4] Quim Peña,[1] Roman Barmin,[1] Felix Gremse,[5] Robert Pola,[6] Michal Pechar,[6] Tomáš Etrych,[6] Steffen Meurer,[7] Ralf Weiskirchen,[7] Rafael Kramann,[3] Fabian Kiessling,[1] Gert Storm,[2,8,9] Josbert Metselaar,[1] and Twan Lammers[1,10,*]

[1]Institute for Experimental Molecular Imaging (ExMI), RWTH Aachen University Clinic, 52074 Aachen, Germany
[2]Department of Pharmaceutics, Utrecht Institute for Pharmaceutical Sciences (UIPS), Utrecht University, 3584 CG Utrecht, the Netherlands
[3]Department of Nephrology and Clinical Immunology, RWTH Aachen University Clinic, 52074 Aachen, Germany
[4]Institute for Pathology, RWTH Aachen University Clinic, 52074 Aachen, Germany
[5]Gremse-IT GmbH, Aachen, Germany
[6]Institute of Macromolecular Chemistry, Academy of Sciences of the Czech Republic, 16200 Prague, Czech Republic
[7]Institute of Molecular Pathobiochemistry, Experimental Gene Therapy and Clinical Chemistry (IFMPEGKC), RWTH Aachen University Clinic, 52074 Aachen, Germany
[8]Department of Targeted Therapeutics, MIRA Institute for Biomedical Technology and Technical Medicine, University of Twente, 7500 AE Enschede, the Netherlands
[9]Department of Surgery, Yong Loo Lin School of Medicine, National University of Singapore, Singapore 119228, Singapore
[10]Lead contact
*Correspondence: tlammers@ukaachen.de
https://doi.org/10.1016/j.celbio.2025.100051

THE BIGGER PICTURE Systemic cancer therapy faces major challenges due to the complex tumor microenvironment, where inflammation-driven abnormalities, such as poor vascular perfusion and excessive extracellular matrix deposition, hinder drug delivery and efficacy. This study demonstrates that liposomal dexamethasone can be employed to beneficially modulate the tumor microenvironment in desmoplastic tumors, enhancing the accumulation and efficacy of drugs and drug delivery systems. Unlike free dexamethasone, liposomal dexamethasone efficiently targets and inhibits profibrotic tumor-associated macrophages, and it thereby primes the tumor vasculature and extracellular matrix for improved drug delivery and treatment efficacy. By integrating nanomedicine-based pharmacological tumor priming in systemic cancer therapy, it may be possible to significantly improve the outcome of drug treatments. Given that liposomal glucocorticoids have already been shown to be effective and safe in patients with rheumatoid arthritis, uveitis, atherosclerosis, and multiple myeloma, translating this concept to the clinic for tumor (and metastases) priming seems a realistic and promising approach.

SUMMARY

Inflammation is a hallmark of cancer. It contributes to a heterogeneous, hyperpermeable, and poorly perfused tumor vasculature, as well as to a dense and disorganized extracellular matrix, which together negatively affect drug delivery. Reasoning that glucocorticoids have pleiotropic effects, we use clinical-stage dexamethasone liposomes (LipoDex) to prime the tumor microenvironment for improved drug delivery and enhanced treatment efficacy. We show that LipoDex priming improves tumor vascular function and reduces extracellular matrix deposition. Single-cell sequencing corroborates LipoDex-mediated inhibition of pro-inflammatory, pro-angiogenic, and pro-fibrogenic gene expression in mononuclear cells, tumor-associated macrophages, and cancer-associated fibroblasts. Multimodal optical imaging illustrates that LipoDex pre-treatment increases the tumor accumulation and intratumoral distribution of subsequently administered polymeric and liposomal drug delivery systems. Using Doxil as a prototypic nanodrug, we finally show that LipoDex priming promotes antitumor treatment efficacy. Altogether, our findings demonstrate that desmoplastic tumors can be primed for improved drug targeting and therapy using clinical-stage glucocorticoid liposomes.

INTRODUCTION

The heterogeneous tumor microenvironment (TME), marked by irregularities in vascular morphology and function and by a typically dense extracellular matrix (ECM) deposition, poses a formidable barrier for anticancer drug delivery and therapy.[1–3] Abnormalities in the TME include heterogeneous vessel distribution, vessel compression, and poor vessel perfusion, together impeding the accumulation and distribution of drugs and drug delivery systems (DDSs) in tumors.[4–6] The dense ECM exacerbates this situation, by increasing the hydrostatic pressure in tumors, hindering extravasation, distribution, and penetration of drugs and DDS, thus negatively affecting the therapeutic performance of pharmacological agents.[4–6]

To overcome TME barriers, several pharmacological and physical priming strategies are being explored, including the use of low-dose antiangiogenic agents, anti-fibrotic agents, and physical pretreatments based on hyperthermia, radiation, and ultrasound.[6,7] Physical TME modulation strategies are highly appealing for local tumor treatment, but not suitable for overcoming barriers in difficult to reach malignancies and metastatic lesions.[7] In such situations, pharmacological or physiological tumor priming is needed.

Inflammation plays a pivotal role in tumorigenesis.[8] During tumor progression, cancer cells manipulate infiltrating immune cells to remodel the tumor ECM.[9] Among the immune cells in tumors, macrophages are particularly abundant, and they have been prominently linked to angiogenesis, tumor progression, and metastasis.[9,10] Tumor-associated macrophages (TAMs) also contribute to ECM deposition, through the activation and trans-differentiation of smooth muscle cells into desmoplastic fibroblasts, as well as through collagen deposition and crosslinking.[3,11–13] In this regard, particularly secreted phosphoprotein-1 (SPP1)-expressing macrophages, also termed as scar-associated macrophages, have crucial role in fibrosis development in various diseases, including in cancer and COVID-19.[14–17]

Targeting TAM with potent anti-inflammatory drugs may help lower the ECM burden, thereby eventually improving drug delivery to and drug distribution in tumors. Glucocorticoids (GCs) are highly potent immunomodulatory agents which are routinely used in the clinic for the management of many different diseases, including various cancers.[18,19] In multiple myeloma, the GC drug dexamethasone (Dex) is used as part of induction therapy, typically combined with chemotherapy and anti-CD38 antibody-based treatment.[20,21] GC act via GC receptors that are abundantly expressed in a range of tissues, explaining their broad spectrum of therapeutic applications and side effects. One of the key adverse effects of GC is their potent catabolic activity at the level of connective tissue production and maintenance. This can lead to pathological conditions such as osteoporosis and skin atrophy, depending on GC dose and exposure time.[22–24]

Taking the above notions into account, we hypothesized that high-dose GC delivery to tumors via liposomes can be exploited to reduce the dense ECM in desmoplastic tumors, exploiting their catabolic capacities, and thereby improving the accumulation, penetration, and efficacy of subsequently administered drugs and DDSs. PEGylated liposomes are known to efficiently target GC to sites of inflammation, as well as to reduce GC exposure in off-target tissues.[25] Accordingly, TAM-targeted liposomal GC delivery holds promise for pharmacological tumor priming. We here used the highly desmoplastic MLS human ovarian cancer model[26–28] and clinical-stage Dex liposomes (i.e., LipoDex)[29–32] to evaluate the effect of LipoDex priming on the TME, on the tumor-directed delivery of clinically relevant polymeric and liposomal nanocarriers, and on the therapeutic performance of clinically used PEGylated liposomal doxorubicin (i.e., Doxil) (Figure 1).

RESULTS

LipoDex treatment modulates TAM and tumor vasculature

We studied TME modulation in the highly stromal MLS ovarian cancer model, which exhibits the highest levels of collagen deposition among a panel of 10 different tumor models routinely used in our lab (Figure S1).[26–28] For tumor priming, we employed a well-characterized and long-term-stable LipoDex formulation (Figure S2), which we recently tested in a first-in-human clinical trial at the CTC-A (Center for Translational & Clinical Research) in Aachen in patients with multiple myeloma.[29] Mice bearing established subcutaneous MLS tumors were intravenously treated (weekly for 3 weeks) with saline, 2.5 mg/kg free Dex, and three different doses of LipoDex (2.5, 5, and 10 mg/kg; Figure 2A). In comparison with saline-treated controls, only the 10 mg/kg LipoDex treatment showed a delay in tumor growth after day 12 and the differences at day 18 were found to be significant as compared to the control (Figure 2B). The difference was only significant for the LipoDex 10 mg/kg group. Additionally, the body weight of mice was significantly reduced upon treatment with LipoDex at a dose of 10 mg/kg (Figure 2C).

TAM are the most prevalent immune cells in tumors, and they are involved in inflammation, angiogenesis, ECM orchestration, and tumor progression.[10,11] GC have been shown to affect TAM genomically and non-genomically, thereby phenotypically and functionally changing their properties.[33–35] We started off analyzing TAM area fraction and total number in MLS tumors via F4/80 staining (i.e., a pan-macrophage marker), observing a dose-dependent depletion in the case of LipoDex, which was statistically significant for the 10 mg/kg dose (Figures 2D, 2H, and S3). These findings are consistent with the reports showing that GC and liposomal GC can deplete macrophages at sites of inflammation.[36–38] We next visualized and quantified Dex and LipoDex effects on SPP1-expressing TAM, because of their prominent involvement in ECM deposition.[15,16] Figures 2E, 2F, 2I, and 2J show a significant decline in SPP1-positive TAM, already upon treatment with the lowest dose of LipoDex. For free Dex, the SPP1-positive TAM population remained unaffected (Figures 2I and 2J). To which extent these effects are mediated via genomic vs. non-genomic effects of GCs needs to be assessed in follow-up studies. Additionally, we analyzed the level of M2-like macrophages via immunofluorescence staining of the mannose receptor C-type 1 (MRC-1), revealing that the majority of TAM in MLS exhibit an M2-like phenotype and that LipoDex treatment induced a strong and dose-dependent depletion of M2-like macrophages (Figure S4).

CellPress
OPEN ACCESS

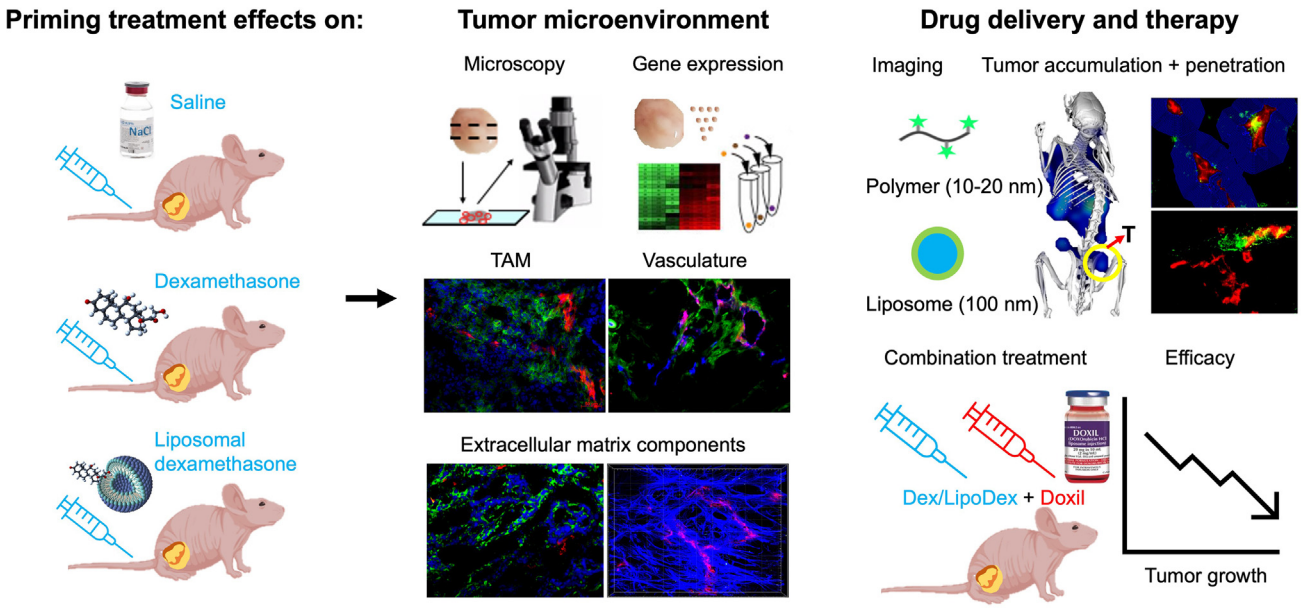

Figure 1. Study design

The potential of LipoDex to modulate the TME and improve tumor-targeted drug delivery was assessed in a highly stromal MLS ovarian cancer mouse model. First, the effects of free Dex and LipoDex priming on cellular (TAM and fibroblast) and structural (vessels, hyaluronan, and collagen) components of the TME were studied, by performing histology and scRNA-seq.

Next, the effects of free Dex and LipoDex priming on the tumor accumulation and penetration of fluorophore-labeled 10–20 nm-sized polymeric and 100 nm-sized liposomal nanocarriers were assessed, using multimodal and multiscale optical imaging. In addition, the effect of free Dex and LipoDex priming on the therapeutic efficacy of Doxil was assessed.

As TAM are involved in angiogenesis via multiple mechanisms,[10] we next analyzed the effect of LipoDex treatment on the morphological and functional characteristics of the tumor vasculature. We stained CD31 as an endothelial cell marker and smooth muscle actin (αSMA) as a marker for pericyte-covered mature blood vessels (Figure 2G). In the 10 mg/kg LipoDex group, a strong and significant decrease in CD31-positive vessel density was observed (Figure 2K), nearly a 2-fold reduction as compared to the control group. Conversely, in the free Dex 2.5 mg/kg group, we found a slight but significant increase in CD31-positive vessels, although the levels of αSMA-positive mature vessels were unaltered as compared to control (Figures 2K and 2L). An increase in αSMA-positive vessels was observed for 5 and 10 mg/kg LipoDex (Figure 2L). For the lowest LipoDex dose, a trend toward improved vessel maturation was noted, which was very close to statistical significance (p = 0.051 vs. control). In line with these findings, we observed increases in the fraction of lectin-positive functional blood vessels; however, values were only found to be significant for the 10 mg/kg LipoDex group (Figure 2M).

To mechanistically explore the tumor priming effects of LipoDex, we next performed single-cell RNA sequencing (scRNA-seq). We only did this for the saline control and 2.5 mg/kg LipoDex groups. For scRNA-seq analysis, murine host cells were sorted via flow cytometry (Figure S5). After normalization and feature selection, clustering showed six different cell population (Figure 2N). The clusters were annotated using single-cell cluster-based automatic annotation toolkit for cellular heterogeneity (scSCATCH) and curated marker genes (Figures 2N and S6). Among these cell clusters, we studied mononuclear phagocyte cells (MPCs), TAMs, and fibroblasts. Functional enrichment analysis of TAM cluster revealed a significant downregulation of transforming growth factor beta (TGF-β) signaling in the top five pathways affected by LipoDex treatment. This pathway is crucially involved in macrophage chemotaxis, polarization, angiogenesis, and ECM production (Figure 2O; Data S2).[39,40] In case of MPC, none of the relevant pathways appeared in the top five downregulated pathways by LipoDex treatment. Nonetheless, the expression of key pro-inflammatory, proangiogenic, and pro-fibrogenic genes such as *Csf1*, *Nfkb2*, *Jak3*, *Nlrc3*, *Angpt2*, *Ang*, *Egln2*, *Bgn*, *Ecm1*, *Col1A1*, *Smad3*, and *Cdk9* were found to be significantly downregulated in both TAM and MPC in the LipoDex 2.5 mg/kg group (see Figures S7A and S7B and Data S1 for details and full gene names). In line with this, the levels of phosphorylated SMAD2/3, which plays a key role in TGF-β-mediated pro-fibrosis signaling, were reduced in the LipoDex 2.5 mg/kg group as compared to both the free Dex 2.5 mg/kg and the control group (Figure S11C).

These initial tumor priming experiments show that a clinical-stage LipoDex formulation affects tumor growth, depletes TAM, inhibits angiogenesis, and normalizes the tumor vascularization when given at a high 10 mg/kg dose. When administered at a low 2.5 mg/kg dose, it does not significantly deplete TAM and normalize blood vessels, but it does reduce the number of $SPP1^+$ pro-fibrogenic TAM, and it does suppress the expression of several relevant genes related to inflammation, angiogenesis, and ECM deposition.

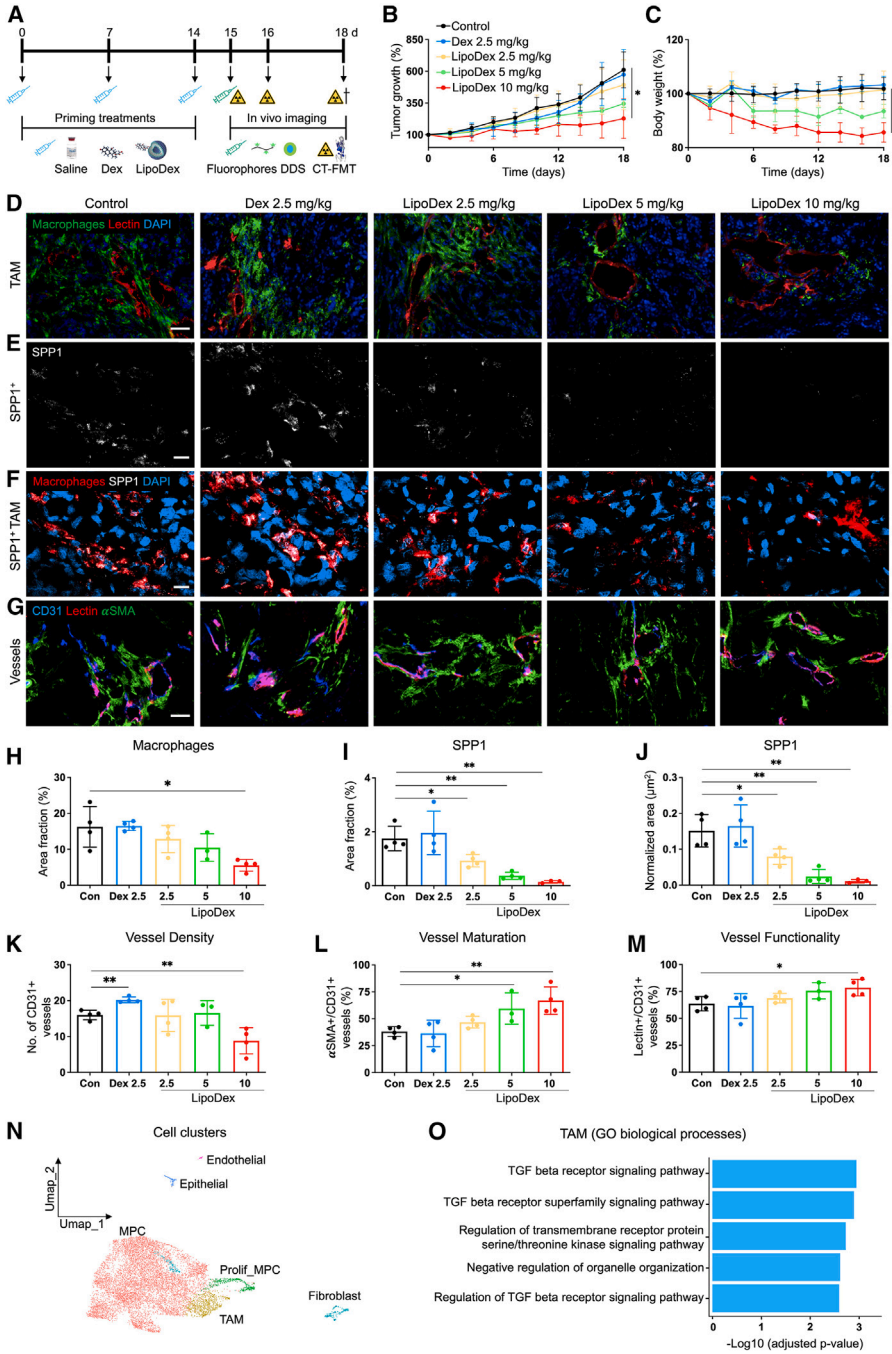

Figure 2. LipoDex treatment modulates TAM and tumor vasculature

(A) Experimental setup.

(B) Relative MLS tumor growth in mice treated with saline, free Dex, and three doses of LipoDex (n = 9–3).

(C) Relative body weight loss (n = 9–3).

(D–G) Immunofluorescence images of F4/80 as a pan-macrophage marker (D), SPP1 as a pro-fibrogenic macrophage marker (E and F), and CD31, rhodamine-lectin, and αSMA as markers for all, perfused, and pericyte-covered vessels, respectively (G).

(H–J) Area fractions of F4/80 (H), SPP1 (I), and normalized area fraction of SPP1 (J) indicate dose-dependent depletion of TAM and SPP1$^+$ TAM by LipoDex.

(K–M) Quantification of tumor blood vessel density (K), vessel maturation (L), and vessel functionality (M).

(N) UMAP plots show distinct clusters of cells in control and 2.5 mg/kg LipoDex-treated tumor.

(O) The top five significantly downregulated biological processes in TAM by 2.5 mg/kg LipoDex treatment include pathways associated with TGF-β signaling (all $p \leq 0.05$). Values represent average ± SD. In (B) and (C), statistical analysis was performed using one-way ANOVA with Tukey's multiple comparisons test. In (H)–(M), two-tailed t test were performed. ns > 0.05, $^*p \leq 0.05$, and $^{**}p \leq 0.01$, and $^{***}p \leq 0.001$. Scale bars represent 50 μm (D and G) and 20 μm (E and F).

LipoDex treatment reduces ECM deposition

Fibrotic ECM components such as hyaluronan and collagen are major barriers, impeding the penetration of drugs and DDSs in tumors.[2,6] Therefore, we next analyzed how free Dex and LipoDex affect ECM deposition in MLS tumors. Immunofluorescence analysis of platelet-derived growth factor receptor beta (PDGFRβ), a marker of fibroblast, showed a significant depletion of cancer-associated fibroblasts (CAFs) by LipoDex in a dose-dependent manner (Figures S8A and S8B). Unlike free Dex, we found a strong and significant reduction in hyaluronan-positive area fraction for all three LipoDex doses (Figures 3A and 3D). Similarly, a dose-dependent and significant reduction in collagen deposition was observed for LipoDex (Figures 3B, 3C, 3E, and 3F). *In vitro* tumor spheroids were used to validate these findings. Heterospheroids of MLS cancer cells and NIH fibroblasts were treated with free Dex and LipoDex for 3 and 7 days, at two different doses. In line with our *in vivo* observations, LipoDex significantly reduced collagen deposition (Figures S8C and S8D). The *in vitro* 3D spheroid experiments furthermore demonstrate a significant reduction in collagen production also by free Dex treatment, suggesting that *in vivo*, the levels of free Dex were insufficiently high to achieve similar effects as those observed with long-circulating LipoDex.

As for TAM (Figure 2O), we also performed biological pathway and gene expression analysis in CAF clusters obtained from control and LipoDex-treated tumors. Consistent with our findings of decreased ECM production following LipoDex treatment, functional enrichment analysis of the CAF cluster revealed that four of the top five significantly downregulated pathways were related to ECM deposition in response to 2.5 mg/kg LipoDex treatment (Figure 3G; Data S3). Additionally, in line with Figures S8A and S8B, cell cluster ratio analysis revealed that LipoDex significantly depleted CAF/fibroblasts (Figure S9A). Furthermore, the expression of genes associated with ECM deposition such as *Col1a1*, *Tnc*, *Fn1*, *Serpinh1*, *Lox*, *Cd44*, and *Vcan* were found to be significantly downregulated in fibroblast cluster in the LipoDex 2.5 mg/kg group compared to the control (Figure S9B and Data S1 for details and full gene names). Together, these findings demonstrate that in tumors, LipoDex more potently reduces ECM deposition than free Dex.

LipoDex priming improves tumor-targeted drug delivery

Based on the notion that LipoDex priming reduces tumor inflammation (Figure 2), modulates tumor vasculature (Figure 2), and decreases ECM deposition (Figure 3), we presumed that tumors are more accessible for nanomedicine targeting. To study this, we treated MLS tumor-bearing mice with saline, Dex (2.5 mg/kg), and LipoDex (2.5, 5, and 10 mg/kg) once a week for 3 weeks. 24 h after the final treatment, mice were intravenously injected with 10–20 nm fluorophore-labeled poly-(*N*-2-hydroxypropyl)methacrylamide (PHPMA) polymers or 100 nm PEGylated liposomes. Mice were subjected to non-invasive whole-body micro-computed tomography-fluorescence molecular tomography (μCT-FMT) imaging at 0, 4, 24, and 72 h time points post intravenous (i.v.) administration[41] (Figure 2A).

We first evaluated the effect of the different doses of LipoDex on the tumor targeting of polymeric nanocarriers (Figure 4). The CT-FMT images in Figure 4A represent the biodistribution and tumor accumulation of PHPMA polymers, showing that priming with LipoDex enhances tumor targeting only at a dose of 2.5 mg/kg (Figure 4B). The mean fractions of polymer tumor accumulation at 72 h after i.v. administration were 3.1% ± 0.5%, 4.7% ± 0.9%, 3.1% ± 0.6%, and 2.1% ± 0.6% injected dose (ID) per 400 mm^3 tumor volume (i.e., the average volume of tumors in this experiment) for the control, LipoDex 2.5, 5, and 10 mg/kg group, respectively.

To assess the impact of LipoDex-based TME priming on the tumor penetration of 10–20 nm-sized polymeric drug carriers, we visualized and analyzed their fluorescence intensity within a 60 μm perimeter around lectin-positive functional blood vessels. As illustrated in Figures 4C and 4D, in saline-treated control tumors, 35.2% ± 11.3% of polymers were found within or directly proximal to vessels. This fraction could be significantly reduced by LipoDex priming, to 16.3% ± 7.2% (p = 0.01 vs. control), 8.8% ± 2.2% (p = 0.001), and 7.3% ± 1.5% (p = 0.002) in the LipoDex 2.5, 5, and 10 mg/kg treatment groups, respectively. In the deepest tissue compartment, located 40–60 μm away from the tumor blood vessel surface, the polymer fraction was found to be significantly higher in the LipoDex groups compared to the control group. The largest overall increase was observed for 5 mg/kg group of LipoDex, with a value of 45.9% ± 4.7% vs. 11.4% ± 3.9% for control.

Up to this point, our primary objective was to assess the effects of different doses of LipoDex on nanocarrier tumor targeting. We next set out to examine whether LipoDex, administered at optimal dose, can also enhance the tumor accumulation of 100 nm-sized liposomes. For this purpose, based on our *in vivo* findings (Figure 4), we employed LipoDex at a dose of 2.5 mg/kg and compared it head-to-head with free Dex administered at an identical dose.

We found that LipoDex enhanced the tumor accumulation of fluorophore-labeled PEGylated liposomes as compared to both saline control and free Dex (Figures 5A and 5B). At 24 h, mean tumor accumulation values of 3.8% ± 1.0%, 2.7% ± 1.0%, and 6.2% ± 1.0% ID per 400 mm^3 were obtained for control, free Dex, and LipoDex, respectively. These values dropped to 2.6% ± 1.2%, 1.2% ± 0.6%, and 5.5% ± 0.5% ID per 400 mm^3 at 72 h, but also at this time point, LipoDex was significantly more potent than free Dex in promoting nanomedicine tumor targeting (Figures 5A and 5B). Interestingly, we also observed at this final time point that the tumor accumulation of fluorophore-labeled PEGylated liposomes was 2-fold lower upon free Dex treatment than upon control treatment (and 4-fold lower than LipoDex treatment; Figure 5B).

As for the smaller-sized polymers, we also analyzed liposome penetration out of tumor blood vessels into the interstitium. Consistent with the observed ECM-related histological (Figure 3) and *ex vivo* polymer penetration findings (Figures 4C and 4D), we detected significantly enhanced liposome penetration upon LipoDex priming (Figures 5C and 5D). Within the first 20 μm surrounding the blood vessel compartment, 56.9% ± 6.4%, 74.3% ± 6.9%, and 49% ± 9.0% of liposomes were retained in untreated, Dex, and LipoDex pretreated tumors, respectively. In the deepest compartments, located 40–60 μm away from the vessel surface, the fraction of liposomes was 27.3% ± 4.7% for the LipoDex-treated group, as compared to 17.9% ± 2.8%

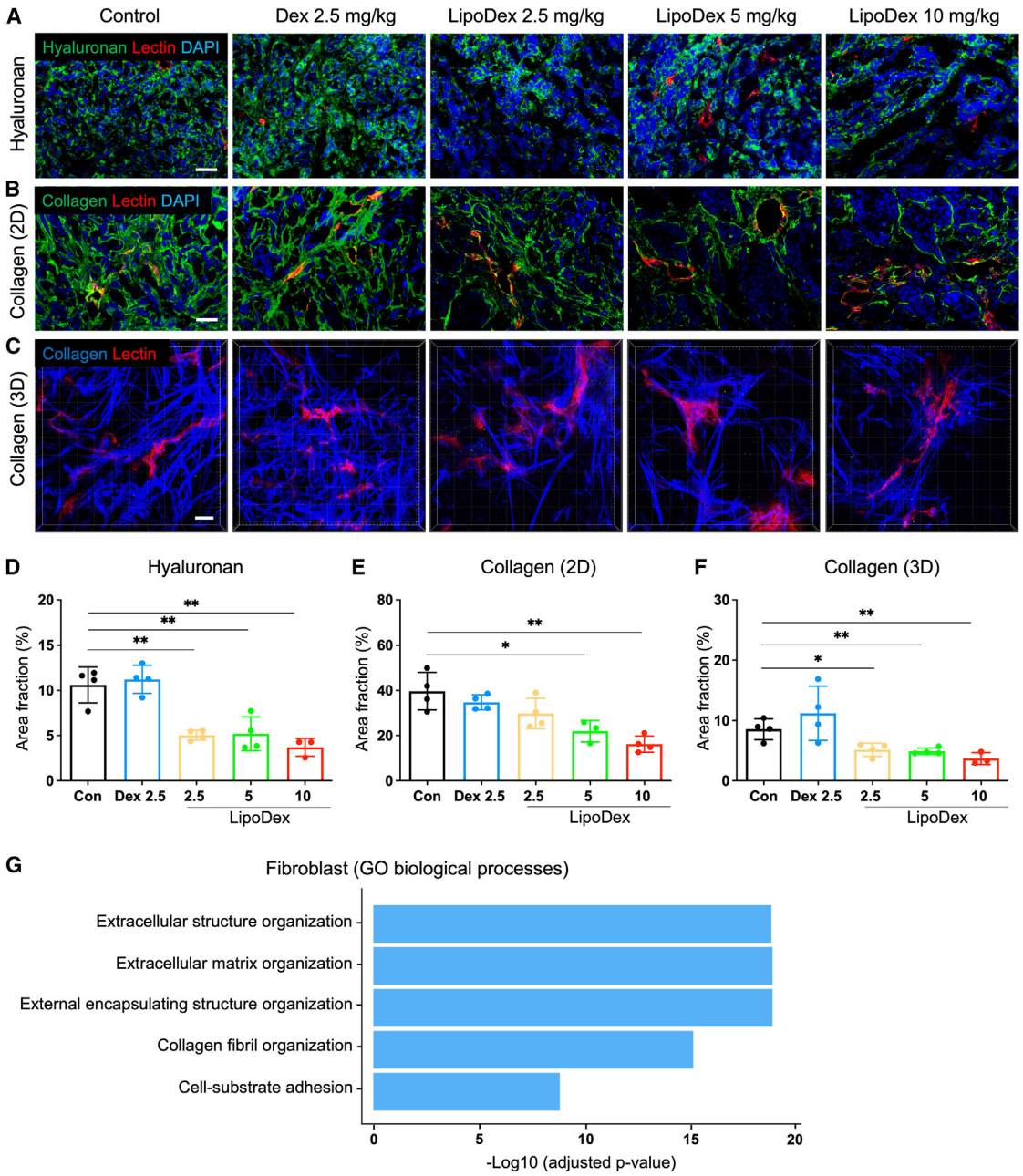

Figure 3. LipoDex treatment reduces ECM deposition

(A and B) Immunofluorescence microscopy analysis of hyaluronan (A) and collagen I (B).

(C) Two-photon microscopy images of collagen fibers, obtained via second-harmonic generation imaging.

(D–F) Quantifications of hyaluronan (D), collagen I (E), and total collagen content in two-photon microscopy (F), exemplifying that even low-dose LipoDex treatment significantly reduces ECM deposition in MLS tumors.

(G) Top five significantly downregulated biological processes in CAFs by 2.5 mg/kg LipoDex treatment include ECM associated pathways (all $p \leq 0.05$). Values represent average ± SD. For (D)–(F), two-tailed t tests were performed; ns > 0.05, $^{*}p \leq 0.05$, and $^{**}p \leq 0.01$. Scale bars represent 50 μm.

($p = 0.008$) for control and 9.6% ± 4.3% ($p = 0.0001$) for free Dex (Figure 5D). These findings thus corroborate the priming potential of LipoDex, showing significant enhancement of tumor accumulation and tumor penetration for both 10–20 nm polymers and 100 nm liposomes.

LipoDex priming enhances cancer nanomedicine treatment efficacy

At a dose of 2.5 mg/kg, LipoDex improves the accumulation and penetration of nanocarriers (Figures 4 and 5), without causing side effects and without intrinsically inducing tumor growth

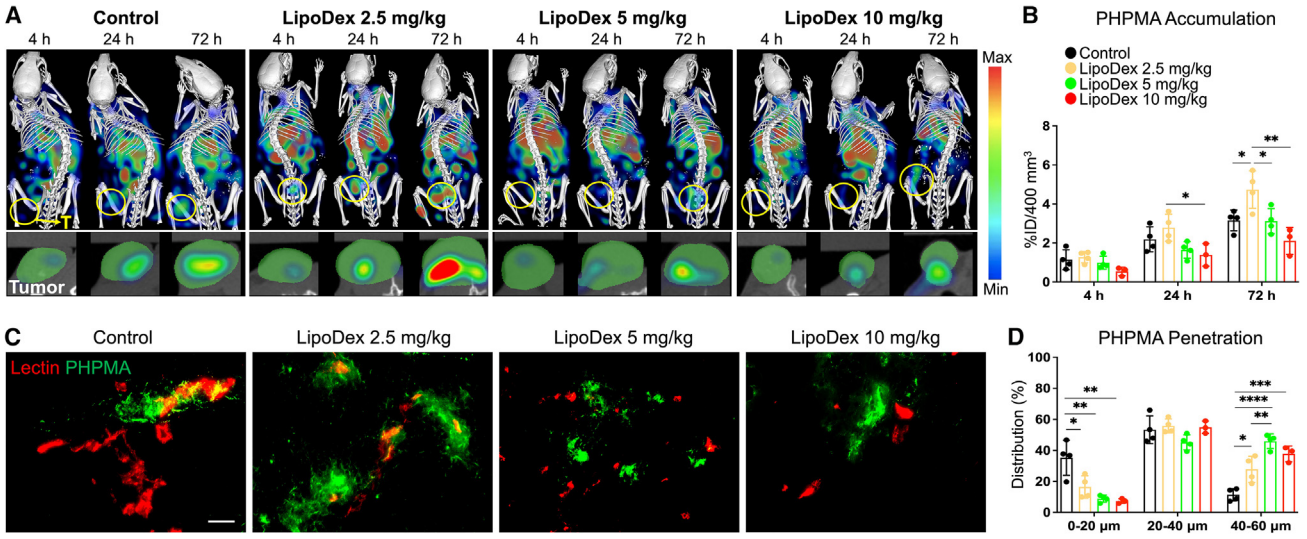

Figure 4. LipoDex priming improves the tumor accumulation and penetration of polymeric nanocarriers

(A) Top: whole-body CT-FMT images showing longitudinal PHPMA biodistribution and tumor accumulation in MLS tumor-bearing mice. Bottom panel: CT-segmented tumor slices (in green) exemplify FMT-assessed polymer accumulation (color-coded clouds).

(B) Normalized PHPMA tumor accumulation quantification in control vs. LipoDex-treated mice, exemplifying that the 2.5 mg/kg dose of the liposomal GC improves polymer tumor targeting.

(C) Fluorescence microscopy analysis of polymer extravasation and penetration out of lectin-stained tumor blood vessels into the interstitium.

(D) Quantification of PHPMA intratumoral distribution reveals that all LipoDex doses enhance polymer penetration as compared to the saline-treated controls. Values represent average ± SD. One-way ANOVA with Tukey's multiple comparisons test was performed for statistical analysis. ns > 0.05, $^{*}p \leq 0.05$, $^{**}p \leq 0.01$, $^{***}p \leq 0.001$, and $^{****}p \leq 0.0001$. Scale bar represents 50 μm.

inhibition (Figures 2B and 2C). We consequently used this 2.5 mg/kg dose to study the therapeutic potential of pharmacological tumor priming with liposomal glucocorticoids. To this end, the antitumor efficacy of the prototypic cancer nanomedicine formulation Doxil (i.e., PEGylated liposomal doxorubicin; administered once weekly for 3 weeks at a dose of 5 mg/kg; Figure 6A) was evaluated with and without free Dex and LipoDex priming at 2.5 mg/kg. An interval of 2 days was maintained between priming and nanochemotherapy. In the monotherapy groups, saline was injected instead of Dex, LipoDex, and Doxil.

In good agreement with improved nanocarrier targeting to and into tumors (Figures 4 and 5), we found that LipoDex priming potently enhanced Doxil treatment efficacy (Figures 6B–6I). Importantly, while it significantly improved Doxil responses, LipoDex itself did not have antitumor activity of its own (Figures 6B, 6E, 6F, 6H, and 6I), corroborating the results reported in Figure 2B. Remarkably, in the case of free Dex, we observed a decline in Doxil performance (Figures 6B, 6F, 6G, and 6I), which is in line with the reduced tumor accumulation of PEGylated liposomes upon free Dex priming (Figure 5). CT-segmented tumor volumes obtained at day 17 exemplify the superior efficacy of the LipoDex + Doxil combination regimen (Figure S10A). Furthermore, all treatments were well tolerated, as evidenced by the lack of body weight loss in the treated mice (Figure S10B) and the absence of physical or behavioral abnormalities observed throughout the treatment period.

Finally, for validation purposes, we analyzed collagen I levels as well as Doxil/doxorubicin accumulation in tumor sections from the respective treatment groups at the end of the experiment. We observed a 2- to 3-fold decrease in collagen deposition for LipoDex + Doxil combination treatment as compared to the Doxil and Dex + Doxil groups (Figures 6J and 6M). Accordingly, we detected higher levels of doxorubicin accumulation in the LipoDex + Doxil combination group as compared to Doxil alone and to free Dex + Doxil (Figures 6K, 6N, and S10C). As a result of priming and improved (nano) drug delivery, we also observed significantly higher levels of apoptosis and DNA damage upon LipoDex + Doxil combination treatment, as evidenced by immunofluorescence staining and quantification of caspase-3 as a marker of apoptosis (Figures 6L and 6O) and phosphorylated histone H2A.X as a marker of DNA damage (Figures S11A and S11B). Western blot analysis of phosphorylated H2A.X confirmed increased DNA damage induction by LipoDex + Doxil (Figure S11C). LipoDex treatment alone did not induce a significant increase in apoptosis or DNA damage as compared to saline, showcasing that the increase in cell death induction as a result of combining LipoDex with Doxil can be solely attributed to LipoDex-mediated enhancement of Doxil tumor accumulation and penetration.

DISCUSSION

We show that treating desmoplastic tumors with clinical-stage dexamethasone liposomes favorably modulates the TME, enhancing tumor-targeted drug delivery and improving cancer nanomedicine treatment efficacy. Importantly, we demonstrate that the encapsulation of dexamethasone in a nanomedicine

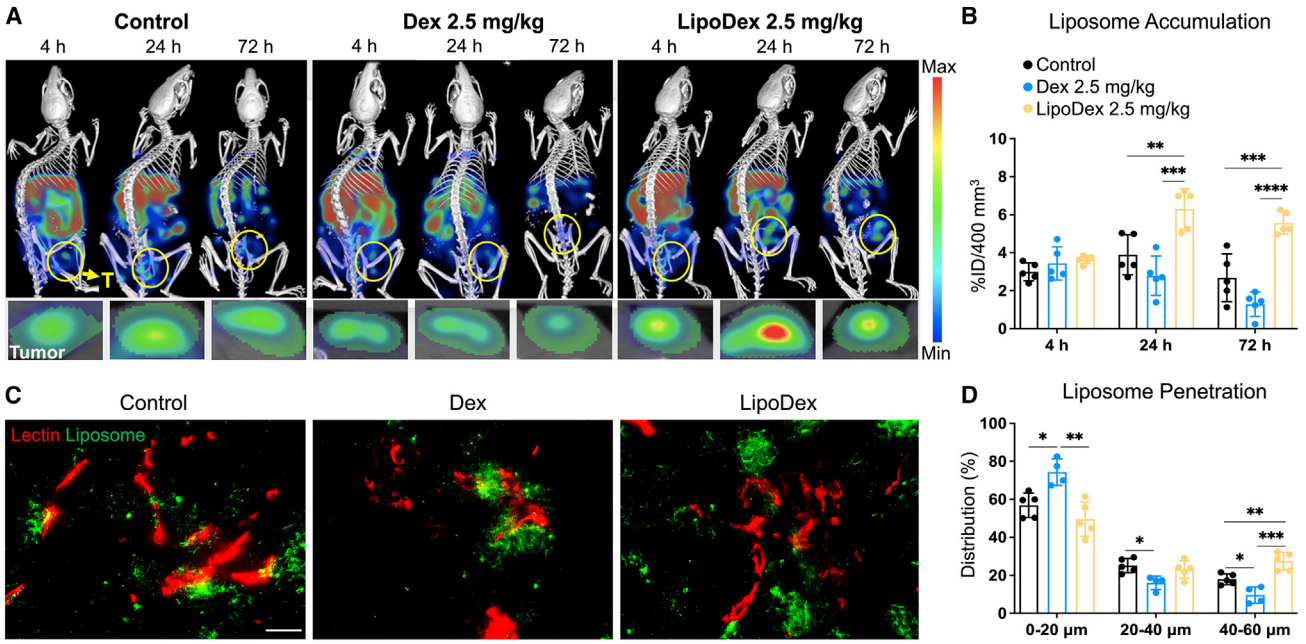

Figure 5. LipoDex priming improves the tumor accumulation and penetration of liposomal nanocarriers

(A) Top: whole-body CT-FLT imaging exemplifies PEGylated liposome biodistribution and tumor accumulation in untreated, free Dex-treated, and LipoDex-treated mice. Bottom panel: CT-segmented tumor slices (green) show liposome tumor accumulation (color-coded clouds).

(B) Quantification of liposome tumor accumulation demonstrates significant enhancement in overall tumor accumulation upon LipoDex priming compared to free Dex treatment and saline controls.

(C) Fluorescence microscopy images depict extravasation and penetration of liposomes out of lectin-labeled tumor blood vessels into the interstitium.

(D) Quantification of intratumoral distribution reveals that LipoDex priming significantly enhances liposome penetration into deeper tumor compartments. Values represent average ± SD. One-way ANOVA with Tukey's multiple comparisons test was performed. ns > 0.05, *$p \leq 0.05$, **$p \leq 0.01$, ***$p \leq 0.001$, and ****$p \leq 0.0001$. Scale bar represents 50 μm.

formulation is required to achieve these effects, outperforming free dexamethasone in almost all regards.

Liposomal glucocorticoids were initially conceived for treating inflammatory disorders, such as rheumatoid arthritis and inflammatory bowel disease.[25,42,43] Subsequently, they were gradually explored for cancer therapy, with experimental evidence showing potent anti-melanoma efficacy in syngeneic mouse models via blocking inflammation and angiogenesis,[34] and with promising proof-of-concept results achieved in mouse models and patients with multiple myeloma.[29,30] Importantly, in multiple myeloma, dexamethasone is routinely used in the clinic as part of first-line induction therapy.[20,21,44,45]

Building upon previous reports showing efficient tumor targeting by liposomal gluocorticoids,[30,31,34] our scRNA-seq and immunohistochemistry analyses demonstrate that LipoDex effectively downregulates TGF-β signaling, suppresses the expression of inflammation-associated genes in TAM (Figures 2O and S7A), depletes SPP1^{+} profibrotic TAM, and normalizes the tumor vasculature (Figures 2E–2M). Histological analysis and *in vivo* imaging revealed the importance of not overdosing LipoDex (Figures 2 and 4). At relatively high doses of 5 and 10 mg/kg, LipoDex very strongly reduced TAM and vessel density. The degree of vessel normalization and relative fraction of perfused blood vessels was the highest for the 10 mg/kg dose, increasing from 60% for control to approximately 75% (Figure 2M); however, when taking into account that the same high dose reduced the total tumor vascular volume by a factor 2 (Figure 2K), it becomes obvious that optimal dosing is required when intending to use LipoDex for desmoplastic tumor priming purposes. With regard to reducing ECM deposition, the dose dependence was less obvious, with all three doses lowering hyaluronan and collagen levels (Figure 3). In line with these notions, an optimal dose of 2.5 mg/kg of LipoDex was identified, which was able to significantly enhance both the accumulation and the penetration of polymeric and liposomal nanomedicines in tumors (Figures 4 and 5). These observations are in good agreement with other pharmacological priming approaches, particularly with classical vascular normalization treatments with low to medium doses of anti-angiogenic agents, which when overdosed result in vessel pruning and in a reduction of drug delivery to tumors.[6,46–49] While the current work did not explore doses of LipoDex lower than 2.5 mg/kg, future studies should also explore this approach, as it could potentially achieve comparable or even further improved tumor priming effects at reduced drug exposure.

When comparing LipoDex to free Dex for tumor priming, we observed a clear benefit for the liposomal gluocorticoid formulation, in terms of both enhancing tumor-targeted drug delivery (Figure 5) and promoting cancer nanomedicine treatment efficacy (Figure 6). As a matter of fact, free Dex treatment even reduced the tumor accumulation and penetration of liposomes as compared to untreated controls (Figure 5). In these experiments, we noted that a higher fraction of liposomes tended to get stuck

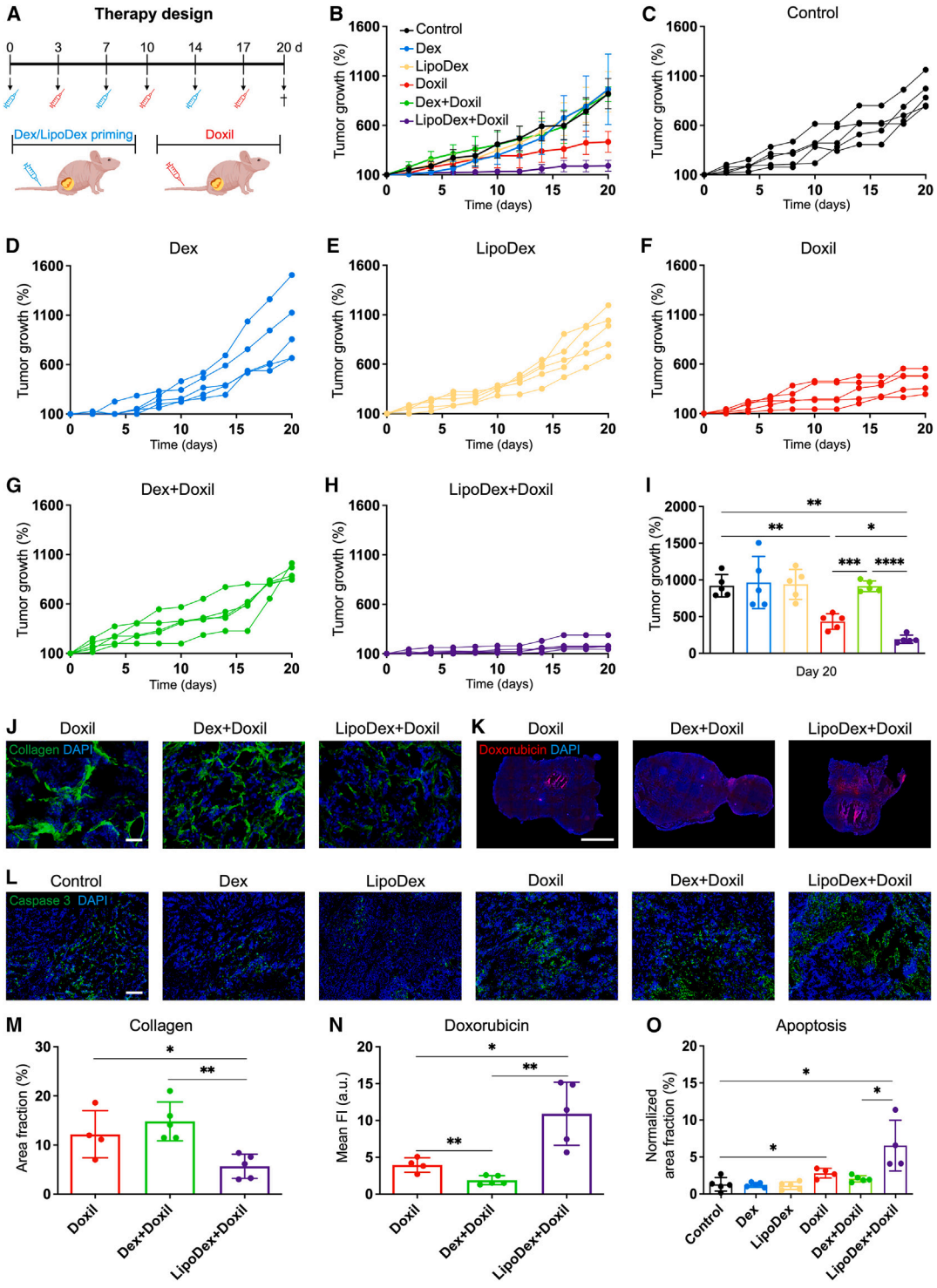

Figure 6. LipoDex priming enhances cancer nanomedicine treatment efficacy

(A) Experimental setup.

(B–H) Tumor growth curves showing that LipoDex boosted the antitumor activity of Doxil, while free Dex negatively affected therapeutic outcome.

(I) Relative tumor volume change at day 20 post therapy start.

(J–O) Fluorescence microscopy analysis of collagen I (J and M), doxorubicin tumor accumulation (K and N), and apoptosis (L and O), substantiating the added value of LipoDex priming. Values represent average ± SD. Brown-Forsythe ANOVA with Dunnett's multiple comparisons test (I) and two-tailed t test were performed (M–O). ns > 0.05, *$p \leq 0.05$, **$p \leq 0.01$, ***$p \leq 0.001$, and ****$p \leq 0.0001$. Scale bars represent 50 μm (J and L) and 2 mm (K).

within the first/vascular compartment (Figure 5D). This suggests that free Dex reduces vessel permeability, at least to some extent, potentially due to pharmacological interference with the tumor endothelium response to vascular endothelial growth factor signaling as a consequence of activation of the glucocorticoid receptor. In line with this, Heiss et al. reported reduced vascular permeability toward albumin in rat glioma tumors upon free Dex treatment.[50] Similarly, Neuwelt et al. observed a significant reduction in the tumor accumulation of methotrexate in glioma lesions upon free Dex treatment,[51] and van der Veldt et al. observed a significant reduction in tumor accumulation of [^{11}C]-docetaxel in patients with lung cancer.[52] These findings concur with our observations (Figure 5), and they may explain why we saw a significant reduction in the antitumor efficacy of Doxil upon combination with free Dex (Figures 6B, 6F, 6G, and 6I). Conversely, when entrapping Dex in liposomes and employing LipoDex for priming purposes, tumor-targeted drug delivery is found to be increased for both 10 and for 100 nm nanocarriers (Figures 4 and 5), as well as for liposome-entrapped doxorubicin (Figures 6K and 6N), thereby prominently promoting the antitumor activity of Doxil (Figures 6B, 6F, 6H, 6I, and 6O).

Recognizing the ECM as a major barrier to tumor delivery underscores the critical need for potent and specific interventions. Efforts to develop small molecules targeting TGF-β and Rho-kinase, which have been the focus of significant recent research, aimed at disrupting ECM deposition, have faced obstacles due to off-target interactions and toxicity,[53] akin to challenges associated with free Dex treatment.[22–25] Since LipoDex—upon initial proof-of-concept studies and good safety observed in patients with multiple myeloma—is now ready for expanded evaluation in clinical trials, we propose to incorporate LipoDex instead of free Dex in combination (chemo)therapy regimens, to help enhance tumor-targeted drug delivery and anticancer therapy outcomes.

METHODS

Materials and formulations

Caelyx (Doxil) was procured from RWTH university hospital pharmacy, and Dex sodium phosphate, pharmaceutical grade (Dex), was obtained from Sigma-Aldrich. The synthesis procedure of PHPMA labeled with ATTO-488 or Dy750 was followed as detailed previously.[41,54] Briefly, in order to prepare fluorophore-labeled PHPMA polymer, (N-2-hydroxypropyl)methacrylamide (HPMA, 85 mol %) and 3-(N-methacryloyl-glycyl-glycyl)thiazolidine-2-thione (Ma-GG-TT, 15 mol %) were copolymerized via radical polymerization in DMSO at 50°C for 6 h. After separation from polymer mixture and characterization the poly(HPMA-co-Ma-GG-TT) was dissolved in N,N′-dimethylacetamide together with the fluorophores ATTO 488-NH2 and Dy750-NH2 in the presence of N,N′-diisopropylethylamine. After 30 min, the polymer was aminolyzed with 1-aminopropan-2-ol, followed by precipitation using diethyl ether. The polymer precipitate was further purified using preparative HPLC (high-performance liquid chromatography) and PD-10 desalting column (GE Healthcare, Solingen, Germany). The content of ATTO 488 (2.1% [w/w]) and Dy750 (1.6% [w/w]) was determine spectrophotometrically. The molecular weight and the polydispersity index (PDI) of PHPMA-Dy750 were 67 and 1.7 kDa, respectively.

BDP-FL- and Cy7-labeled liposomes were prepared by the conventional thin film hydration technique. In short, dipalmitoylphosphatidylcholine (DPPC: 180.6 mg), cholesterol (51.8 mg), poly(ethylene glycol) 2000-distearoyl phosphatidylethanolamine (DSPE-mPEG2k: 56.1 mg), DSPE-3-Bodipy-propanoic acid (DSPE-BDP-FL: 4 mg), and DSPE-Cyanine 7 (DSPE-Cy7: 0.52 mg) were dissolved in chloroform in a round bottom flask. A thin lipid film was prepared by evaporating chloroform in a rotary vacuum for 1h at max vacuum at 70°C. Thin lipid film was then hydrated with 10 mL phosphate-buffered saline, pH 7.4) under 1 h of rotary mixing at 70°C. Liposomes were then downsized by means of extrusion, five times with 200 and 100 nm track-etched polycarbonate membrane filter using a Liposofast LF-50 extruder (Avestin). The hydrodynamic diameter and PDI of LipoDex were measured using dynamic light scattering (DLS, Nano-S, Malvern Panalytical PLC, UK) at 25°C with a fixed scattering angle of 173°, resulting in values of 128 nm and 0.04, respectively.

LipoDex size and morphology were analyzed using DLS and cryogenic transmission electron microscopy (cryo-TEM). The hydrodynamic size of LipoDex was measured using DLS (Nano-S, Malvern Panalytical PLC, UK) at 25°C with a fixed scattering angle of 173°. For cryo-TEM analysis, Quantifoil 1.2/1.3 Cu 200 grids with a 2 nm carbon film (Quantifoil Micro Tools, Germany) were plasma-cleaned and prepared using the VitroJet system (CryoSol-World B.V., the Netherlands). Liposomal samples were applied via pin-printing and vitrified with liquid ethane. Imaging was conducted on a 200 kV Talos Arctica microscope (Thermo Fisher Scientific, MA, USA) equipped with a K3 BioQuantum energy filter at 100,000× magnification, with a pixel resolution of 0.816 Å and a total electron dose of 30 e^{-}/Å^2.

Heterospheroid growth and immunofluorescence image analysis

MLS and mouse embryonic fibroblast (NIH-3T3) cell lines were grown in α-MEM (minimum essential medium alpha modification) and DMEM media, respectively, and both media were supplemented with 10% fetal bovine serum and 1% penicillin/streptomycin. Heterospheroid formation of MLS and NIH cells was attained via the hanging drop method in a 96-well plate. Briefly, trypsinized MLS and NIH were mixed to a 1:1 (v/v) ratio at a density of 6 × 10^5 cells/mL. 20 μL of this suspension containing 12.000 cells were seeded onto the bottom of the inverted lid and spheroids were generated by the well-plate flip technique. After 7 days, spheroids were treated with Dex (0.1 and 5 μM) or LipoDex (0.1 and 5 μM). Spheroids were then collected on day 3 and day 7 post treatments and were further embedded in Tissue-Tek and cryopreserved at −80°C until cryosectioning. For immunofluorescence staining, cryosections (7 μM) were prepared and stained for DAPI and collagen I using collagen I antibody (Novus Biologicals, UK). The stained slides were then glass-covered using Mowiol 4–88 (Carl Roth, Germany). Images of all stained slides were acquired using fluorescence microscopy at a 10× magnification (Axio Imager M2, Carl Zeiss Microscopy, Oberkochen, Germany). For the quantification, collagen area fraction in 3–4 spheroids was analyzed using the AxioVision SE64 Rel. 4.8 software (Carl Zeiss Microscopy, Oberkochen, Germany).

Animal handling and tumor induction

All experiments were performed according to the guidelines of the local and national ethics authorities for animal welfare (German State Office for Nature, Environment and Consumer Protection [LANUV\ North Rhine-Westphalia). 6–8 weeks old, CD-1 BALB/cAnN-Fox1 female nude mice ($n = 31$) were obtained from Charles River. Mice were kept in pathogen-free ventilated cages under a light/dark cycle of 12/12 h. Food and water were given *ad libitum*. 5×10^6 MLS cells (i.e., human ovarian carcinoma) were inoculated subcutaneously on the right flank of the mice. Mice body weight and tumor growth (via caliper measurements) were monitored daily. Mice were randomly assigned to therapy groups (n = 5–3) when tumors reached a size of 4–6 mm in diameter.

Non-invasive imaging protocol and image processing

Mice bearing subcutaneous MLS tumors were pretreated with either saline (NaCl 0.9%) or Dex 2.5 mg/kg or three different doses of LipoDex (i.e., 2.5, 5, and 10 mg/kg) once a week for 3 weeks. 2 days prior to CT-FMT imaging, the regular diet of mice was changed to a chlorophyll-free diet (ssniff Spezialdiäten, Soest, Germany) to reduce background fluorescence in the FMT scan. The day after the last treatment injection, mice were intravenously injected with 2 nM of either ATTO-488-/Dy750-labeled fluorescent PHPMA polymer or BDP-FL-/Cy7-labeled fluorescent liposomes. All the i.v. administrations were done via the tail vein using a catheter with a 30G needle (B.Braun Melsungen, Germany) under anesthesia using 2% isoflurane (Forene, Abbott, Wiesbaden, Germany) in oxygen-enriched air supplied via a dedicated vaporizer. After i.v. administration of fluorophores, anesthetized mice were subjected to CT-FMT scans at 0, 4, 24, and 72 h to longitudinally assess fluorophore tumor accumulation. Initially, mice were scanned using a dual-energy flat-panel μCT scanner (TomoScope 30s Duo, CT-Imaging, Erlangen, Germany), capturing 720 projections with 1,032 × 1,012 pixels in 1.1 full rotation within 90 s. Subsequently, volumetric datasets were reconstructed at an isotropic voxel size of 35 μm using a Feldkamp-type algorithm and a smooth kernel. Following the μCT scan, the mouse bed was transferred to the FMT (FMT 2500 LX, PerkinElmer, MA, USA), and FMT scans were conducted at 750 nm using 115–120 grid points.

For liposome accumulation assessment, the μCT-FLT device (U-CT OI, MILabs B.V., a Rigaku Company, Utrecht, the Netherlands) was utilized. Initially, the animal holder was automatically positioned between the FLT laser and the cooled charge-coupled device (CCD) camera. Scanning was performed using a laser with a 730 nm wavelength and an emission filter (775 + 25 nm) to capture excitation and emission images of approximately 130 laser points. Following the FLT scan, the animal holder was automatically repositioned for CT scanning. A total-body μCT scan was performed with a full rotation in step-and-shoot mode, acquiring 480 projections (1,944 × 1,536 pixels) at an X-ray tube voltage of 55 kV, power of 0.17 mA, and an exposure time of 75 ms, with low-dose radiation (approximately 0.1 Gy/whole-body scan). To cover the entire animal, two subscans were acquired.

After the last CT-FMT or CT-FLT scan, mice were intravenously injected with rhodamine-lectin (to stain blood vessels) and 10 min later, they were sacrificed. Hybrid CT-FMT images were reconstructed and analyzed using Imalytics Preclinical (Gremse-IT, Germany).[55] Based on the analytical information from CT scans, tumors were segmented, and fluorescence signal from FMT or FLT scans, allocated in the tumor region was quantified as % ID per 400 mm^3 tumor volume.

Histology and histological analysis

For each histological staining, cryopreserved tumors (in Tissue-Tek, Sakura Finetek Europe, the Netherlands) were cut into 7 μm-thick sections from three different tumor layers and stored at −80°C until further use. To determine the effect of treatments on macrophages, vasculature, fibroblasts, hyaluronan, collagen I, cell apoptosis, M2-like macrophages, and DNA damage, tumor tissues were stained with, pan-macrophage marker F4/80 (Bio-RaD #MCA497GA), CD31 (endothelial cell marker, BD Biosciences #553370), αSMA (perivascular cells, Progen #BK61501), DAPI (nuclei, Sigma-Aldrich), PDGRβ antibody (Cell Signaling #3169), hyaluronan antibody (Abcam #53842), collagen I antibody (Novus Biologicals #NB600-408), caspase-3 antibody (abcam #ab49822), MRC-1 (Acris #SM1857P), and phosphorylated histone H2A.X (Cell Signaling #97182S), respectively. Additionally, tissue slices were permeabilized with 0.3% Triton X-100 in PBS buffer (pH 7.2) for 7 min to facilitate apoptosis and DNA damage analysis. Images were acquired using the AxioImager M2 microscopy system (Carl Zeiss Microscopy, Oberkochen, Germany). Vascular analyses such as vessel density, vessel maturation, and vessel functionality were analyzed by counting CD31+ vessels (total no. of vessels), calculating % of αSMA positive-CD31 vessels, and rhodamine-lectin-positive CD31 vessels, respectively. TAM, collagen, and hyaluronan turnover were determined in terms of area percent using AxioVision software. *Ex vivo* tumor penetration analysis was done by in 7-μm-thick tissue sections using Definiens Developer XD 2.0.4 software (Germany). Briefly, Definiens rule sets generated concentric rings of different step sizes around the tumor blood vessels (21 rings, corresponding to a total distance of 60 μm away from the blood vessel wall), and in each ring, the fluorescence intensity values of accumulated fluorophore-labeled polymers or liposomes were obtained. From these values, the percentage distribution of polymers and liposomes was then graphically plotted. Doxorubicin or Doxil *ex vivo* tumor accumulation was assessed via acquiring images using the AxioImager M2 microscopy. Fluorescence intensity of accumulated doxorubicin in tumor tissues was measured using ImageJ.

SPP1 RNA *in situ* hybridization

SPP1 RNA ISH on cryopreserved tumors was performed using the RNA-Scope detection kit (Multiplex Fluorescent Reagent Kit v2 Assay) according to the manufacturer's protocol. C3-mSPP1 (435191-C3) was used for SPP1 RNA-hybridization. Pan-macrophage marker F4/80 (Bio-RaD #MCA497GA) immunofluorescence staining was performed. Next, slices were stained with DAPI (1 μg/mL) for 2 min. Sections were mounted with ImmuMount media and covered by coverslips. The hybridized slides were imaged using a Zeiss LSM 980 confocal laser microscope and the acquired images were processed and quantified using Zeiss Zen software.

Western blot

Sample preparation and protein extraction

Two 100 μm cryosections from tumor specimens were thawed on ice. The tissue was carefully extracted with forceps to remove excess Tissue-Tek and placed in RIPA buffer supplemented with complete protease inhibitors (Roche Diagnostics, Mannheim, Germany) and phosphatase inhibitor cocktail II (Sigma-Aldrich). Homogenization was performed using an MM400 ball mill (Retsch, Haan, Germany) with a pre-cooled Eppendorf holder at 30 Hz for 10 min, followed by sonication with three 10-s bursts on ice using an ultrasonic disintegrator (UP100H, Hielscher Ultrasound Technology, Teltow, Germany). The homogenates were sheared using a 27 G needle (0.4 × 20 mm), incubated on ice for 30 min, and centrifuged at 10,000 rpm for 10 min at 4°C. Protein concentration was determined using the DC protein assay (Bio-Rad, Düsseldorf, Germany).

Sodium dodecyl sulfate polyacrylamide gel electrophoresis and western blot analysis

Equal amounts of total protein (60 μg per lane) were mixed with NuPAGE lithium dodecyl sulfate (LDS) sample buffer (Invitrogen, Thermo Fisher Scientific, Dreieich, Germany) containing dithiothreitol (DTT). After denaturation at 70°C for 10 min, proteins were separated on 4%–12% gradient gels using MES running buffer and transferred onto 0.2 μm nitrocellulose membranes with NuPAGE blotting buffer.[56] Proper protein transfer was verified using Ponceau S staining. Membranes were blocked with 5% (w/v) non-fat milk in Tris-buffered saline with 0.1% Tween 20 (TBST). Primary antibodies were diluted in 2.5% (w/v) non-fat milk in TBST and incubated overnight. The following primary antibodies were used: β-actin (AC-15, Sigma, A5441), pSMAD2 (CT, Cell Signaling, CS-8828), and p-Histone H2A.X (Cell Signaling, CS97182S). Detection was performed using anti-mouse, anti-rabbit, or anti-goat IgG secondary antibodies (Santa Cruz Biotech, Santa Cruz, CA, USA) and SuperSignal chemiluminescent substrate (Pierce, Bonn, Germany).

Two-photon laser scanning microscopy

Tumor tissues (100 μm thick) were subjected to two-photon imaging. Images were acquired using a 25× water-immersed objective lens mounted on the Olympus FV1000MPE multiphoton microscopy system. Each image consisted stacks of 50 images with a step size of 1 μm. With this technique, images of tumor blood vessels (rhodamine-lectin stained) and collagen content (via second-harmonic generation imaging) were acquired.[57] The acquired images were then analyzed using Imaris Software, version 7.4 (Bitplane AG, Zurich, Switzerland). By means of intensity thresholding, the relative collagen content was quantified.

scRNA data analysis

scRNA-seq sample preparation

To generate a single-cell solution, tumor samples were minced using a scalpel, over an ice bath. The minced tissue samples were then transferred to 50 mL falcon tubes containing 6 mL digestion medium that contains RPMI 1640 #31870025 with 0.2 mg/mL Liberase TL Research Grade (Roche 5401020001) and 60 U/mL DNase I (Sigma D5025) followed by incubation for 40 min at 200 RPM at 37°C on an orbital shaker. The digestion was stopped by adding 10 mL ice-cold buffer (PBS + 10% fetal bovine serum) and from now on the samples were always kept at 4°C. Next, each sample was filtered through a 100 μm cell strainer, and cells were washed by centrifugation for 5 min at 300 × g and resuspended in 20 mL ice-cold fluorescence-activated cell sorting (FACS) buffer (PBS + 2% fetal bovine serum). Erythrocytes were lysed for 5 min on ice (eBioscience 1X RBC Lysis Buffer, in MilliQ water), and the cells were washed again with 10 mL FACS buffer. To enrich PDGFRβ-positive live cells, the cells were incubated with an anti-mouse PDGFRβ antibody (concentration 1:100, 12-1402-81 eBioscience) and stained with DAPI (Roche, 10236276001). Cells were sorted with a Sony LE-SH800 for DAPI negative, PDGFRβ-positive signal.

Alignment, preprocessing, and quality control

Using the CellRanger analysis pipeline (v7.1.0) from 10x Genomics, we performed alignment to the murine transcriptome (reference sequence GRCm39-2024-A), yielding 5,459 and 5,913 cells and an average of 6,555 and 26,250 reads per cell corresponding a sequencing saturation of 28.3% and 42% in control and LipoDex treatment samples, respectively. The generated filtered gene expression count matrices were used for further downstream analysis. For downstream analysis, we generated a Seurat object (v5.0.2) by using the generated gene expression count matrices as input by the function *CreateSeuratObject*. Here, we filtered for cells containing at least 200 gene features and removed gene features present in 3 or less cells. Further, cells containing less than 200 or more than 5,000 gene features as well as cells containing >10% mitochondrial RNA ("*^mt-*") were excluded. After quality control, we obtained 5,140 and 49,69 cells in control group and LipoDex treatment group, respectively. For data integration of both samples, we used the *merge* function and integrated the data using the *Harmony* integration algorithm.[58] Lastly, we normalized the count matrix using the *NormalizeData()* function ("*LogNormalize*", *scale.factor = 10,000*) and performed data scaling using the *ScaleData()* function. Variable features were identified (*FindVariableFeatures*, features set to 2000, Seurat), and principal components (*RunPCA*, Seurat) were calculated. Optimal dimensions for uniform manifold approximation and projection (UMAP) visualization were determined by generating individual elbow plots. Subsequently, we performed UMAP dimensionality reduction (*RunUMAP*, Seurat) with dimensions set to 25.

Cell clustering

Cell clustering was performed using *FindNeighbors* (dim = 25, Seurat) and *FindClusters* (res = 0.1, Seurat), and we used differential gene expression analysis (*FindMarkers*, Seurat) to identify marker genes. The final cluster annotation was performed manually based on information from actual literature. For further downstream analysis, we subsetted the dataset for the identified clusters of TAM, proliferating MPC, MPC, and fibroblasts.

Gene set enrichment and differential expression analysis

For gene set enrichment analysis, we used the R package gProfileR and restricted analysis for the Gene Ontology database (GO Biological process).[59] Functional enrichment analysis was performed with the gene ontology statistical test (GOST) function of gProfileR setting a p value of 0.05. All genes with $\log_2$ fold

change ≥ 0.1 and adjusted $p \leq 0.05$ were used in the functional enrichment analysis without considering the order of the genes. Differential expression analysis in each cluster was performed using the *FindMarkers* function with the Wilcoxon test.

In vivo therapeutic efficacy study

Mice bearing subcutaneous MLS tumors were randomly assigned to six groups (n = 5/group) when the tumors reached a size of 4–6 mm in diameter. The treatments were administered intravenously via the tail vein using a catheter with a 30G needle (B. Braun, Melsungen, Germany) under anesthesia using 2% isoflurane in oxygen-enriched air supplied via a dedicated vaporizer. Mice were intravenously pretreated with either saline or Dex 2.5 mg/kg or LipoDex 2.5 mg/kg once a week for 3 weeks. 2 days after the pretreatments, mice were intravenously treated with commercially available Doxil (5 mg/kg) or saline once a week for 3 weeks. Right after the last therapy injection (Doxil or saline), mice were subjected to whole-body CT scan (U-CT OI, MILabs B.V., a Rigaku Company, Utrecht, the Netherlands) under anesthesia (2% isoflurane). Mice body weight and tumor growth were monitored daily. Tumor measurements were done manually using a caliper. Mice were sacrificed under anesthesia via cervical dislocation 20 days post the first therapy injection.

Statistical analysis

Statistical analysis was done using GraphPad Prism 9. All the results are presented as average ± standard deviation. Statistical was performed using the two-tailed t test, one-way ANOVA with Tukey's multiple comparison test, and Brown-Forsythe ANOVA with Dunnett's multiple comparisons test. $p \leq 0.05$ were considered to be statistically significant.

RESOURCE AVAILABILITY

Lead contact

Further information and requests for resources and reagents should be directed to and will be fulfilled by the lead contact, Twan Lammers (tlammers@ukaachen.de).

Materials availability

All unique materials/reagents generated in this study are available from the lead contact with a completed materials transfer agreement.

Data and code availability

- All original code and scRNA-seq cell Ranger files have been deposited in Zenodo and are available under the doi: 10.5281/zenodo.14952484.
- Any additional information required to reanalyze the data reported in this paper is available from the lead contact upon request.

ACKNOWLEDGMENTS

The authors gratefully acknowledge financial support by the European Research Council (ERC; 864121 [Meta-Targeting] and 101138100 [PRIME]), the European Union (EU H2020-MSCA-ITN-2014 642028 [NABBA]), the European Union (Next Generation European Union, National Institute for Cancer Research [program EXCELES, ID project no. LX22NPO5102]), the German Research Foundation [LA2937/4-1, RTG2735 [331065168], KFO5011, SFB1066]), and the German Academic Exchange Program (DAAD 5721 4224). Schematic figures were partly created using figures provided by Servier Medical Art (https://smart.servier.com/), licensed under a Creative Commons Attribution 4.0 (https://creativecommons.org/licenses/by/4.0/).

AUTHOR CONTRIBUTIONS

T.L. conceived and supervised the study. Experimental planning, material preparation, and data collection were carried out by T.O., G.J.L.S., R.M., V.P., J.E., E.R., F.D.L., A.S.E., D.M., S.E., B.T., M. Wagner, P.C., L.C., M. Weiler, F.P., T.C., Q.P., R.B., S.M., and F.G. Interpretation of the results was conducted by T.O., G.J.L.S., J.E., F.D.L., S.M., M. Wagner, and T.L. Scientific input was provided by R.P., M.P., T.E., R.W., R.K., F.K., G.S., and J.M. The initial manuscript was drafted by T.O. J.M., G.S., and T.L. provided input, edited, and reviewed the first draft. All authors read and approved the final version of the manuscript.

DECLARATION OF INTERESTS

The authors declare no competing interests.

SUPPLEMENTAL INFORMATION

Supplemental information can be found online at https://doi.org/10.1016/j.celbio.2025.100051.

Received: November 16, 2024
Revised: February 11, 2025
Accepted: March 12, 2025
Published: April 8, 2025

REFERENCES

1. De Lázaro, I., and Mooney, D.J. (2021). Obstacles and opportunities in a forward vision for cancer nanomedicine. Nat. Mater. *20*, 1469–1479. https://doi.org/10.1038/s41563-021-01047-7.
2. Nia, H.T., Munn, L.L., and Jain, R.K. (2020). Physical traits of cancer. Science *370*, eaaz0868. https://doi.org/10.1126/science.aaz0868.
3. Sutherland, T.E., Dyer, D.P., and Allen, J.E. (2023). The extracellular matrix and the immune system: A mutually dependent relationship. Science *379*, eabp8964. https://doi.org/10.1126/science.abp8964.
4. Nguyen, L.N.M., Ngo, W., Lin, Z.P., Sindhwani, S., MacMillan, P., Mladjenovic, S.M., and Chan, W.C.W. (2024). The mechanisms of nanoparticle delivery to solid tumours. Nat Rev Bioeng. *2*, 201–213. https://doi.org/10.1038/s44222-024-00154-9.
5. Mitchell, M.J., Billingsley, M.M., Haley, R.M., Wechsler, M.E., Peppas, N.A., and Langer, R. (2021). Engineering precision nanoparticles for drug delivery. Nat. Rev. Drug Discov. *20*, 101–124. https://doi.org/10.1038/s41573-020-0090-8.
6. Stylianopoulos, T., Munn, L.L., and Jain, R.K. (2018). Reengineering the physical microenvironment of tumors to improve drug delivery and efficacy: from mathematical modeling to bench to bedside. Trends Cancer *4*, 292–319. https://doi.org/10.1016/j.trecan.2018.02.005.
7. Ojha, T., Pathak, V., Shi, Y., Hennink, W.E., Moonen, C.T.W., Storm, G., Kiessling, F., and Lammers, T. (2017). Pharmacological and physical vessel modulation strategies to improve EPR-mediated drug targeting to tumors. Adv. Drug Deliv. Rev. *119*, 44–60. https://doi.org/10.1016/j.addr.2017.07.007.
8. Colotta, F., Allavena, P., Sica, A., Garlanda, C., and Mantovani, A. (2009). Cancer-related inflammation, the seventh hallmark of cancer: links to genetic instability. Carcinogenesis *30*, 1073–1081. https://doi.org/10.1093/carcin/bgp127.
9. Khatami, M. (2014). Chronic inflammation: Synergistic interactions of recruiting macrophages (TAMs) and eosinophils (Eos) with host mast cells (MCs) and tumorigenesis in CALTs. M-CSF, suitable biomarker for cancer diagnosis!. Cancers (Basel) *6*, 297–322. https://doi.org/10.3390/cancers6010297.
10. Hu, W., Li, X., Zhang, C., Yang, Y., Jiang, J., and Wu, C. (2016). Tumor-associated macrophages in cancers. Clin. Transl. Oncol. *18*, 251–258. https://doi.org/10.1007/s12094-015-1373-0.

11. Liguori, M., Solinas, G., Germano, G., Mantovani, A., and Allavena, P. (2011). Tumor-associated macrophages as incessant builders and destroyers of the cancer stroma. Cancers (Basel) *3*, 3740–3761. https://doi.org/10.3390/cancers3043740.

12. Finkernagel, F., Reinartz, S., Lieber, S., Adhikary, T., Wortmann, A., Hoffmann, N., Bieringer, T., Nist, A., Stiewe, T., Jansen, J.M., et al. (2016). The transcriptional signature of human ovarian carcinoma macrophages is associated with extracellular matrix reorganization. Oncotarget *7*, 75339–75352. https://doi.org/10.18632/oncotarget.12180.

13. Afik, R., Zigmond, E., Vugman, M., Klepfish, M., Shimshoni, E., Pasmanik-Chor, M., Shenoy, A., Bassat, E., Halpern, Z., Geiger, T., et al. (2016). Tumor macrophages are pivotal constructors of tumor collagenous matrix. J. Exp. Med. *213*, 2315–2331. https://doi.org/10.1084/jem.20151193.

14. Trinh, H.K.T., Nguyen, T.V.T., Kim, S.-H., Cao, T.B.T., Luu, Q.Q., Kim, S.-H., and Park, H.-S. (2020). Osteopontin contributes to late-onset asthma phenotypes in adult asthma patients. Exp. Mol. Med. *52*, 253–265. https://doi.org/10.1038/s12276-020-0376-2.

15. Hoeft, K., Schaefer, G.J.L., Kim, H., Schumacher, D., Bleckwehl, T., Long, Q., Klinkhammer, B.M., Peisker, F., Koch, L., Nagai, J., et al. (2023). Platelet-instructed SPP1+ macrophages drive myofibroblast activation in fibrosis in a CXCL4-dependent manner. Cell Rep. *42*, 112131. https://doi.org/10.1016/j.celrep.2023.112131.

16. Qi, J., Sun, H., Zhang, Y., Wang, Z., Xun, Z., Li, Z., Ding, X., Bao, R., Hong, L., Jia, W., et al. (2022). Single-cell and spatial analysis reveal interaction of FAP+ fibroblasts and SPP1+ macrophages in colorectal cancer. Nat. Commun. *13*, 1742. https://doi.org/10.1038/s41467-022-29366-6.

17. MacDonald, L., Alivernini, S., Tolusso, B., Elmesmari, A., Somma, D., Perniola, S., Paglionico, A., Petricca, L., Bosello, S.L., Carfì, A., et al. (2021). COVID-19 and RA share an SPP1 myeloid pathway that drives PD-L1+ neutrophils and CD14+ monocytes. JCI Insight *6*, e147413. https://doi.org/10.1172/jci.insight.147413.

18. Aldea, M., Orillard, E., Mansi, L., Marabelle, A., Scotte, F., Lambotte, O., and Michot, J.-M. (2020). How to manage patients with corticosteroids in oncology in the era of immunotherapy? Eur. J. Cancer *141*, 239–251. https://doi.org/10.1016/j.ejca.2020.09.032.

19. Roth, P., Happold, C., and Weller, M. (2015). Corticosteroid use in neuro-oncology: an update. Neurooncol. Pract. *2*, 6–12. https://doi.org/10.1093/nop/npu029.

20. Reeder, C.B., Reece, D.E., Kukreti, V., Mikhael, J.R., Chen, C., Trudel, S., Laumann, K., Vohra, H., Fonseca, R., Bergsagel, P.L., et al. (2014). Long-term survival with cyclophosphamide, bortezomib and dexamethasone induction therapy in patients with newly diagnosed multiple myeloma. Br. J. Haematol. *167*, 563–565. https://doi.org/10.1111/bjh.13004.

21. van de Donk, N.W.C.J., Richardson, P.G., and Malavasi, F. (2018). CD38 antibodies in multiple myeloma: back to the future. Blood *131*, 13–29. https://doi.org/10.1182/blood-2017-06-740944.

22. Adami, G., and Saag, K.G. (2019). Glucocorticoid-induced osteoporosis: 2019 concise clinical review. Osteoporos. Int. *30*, 1145–1156. https://doi.org/10.1007/s00198-019-04906-x.

23. Cutroneo, K.R., and Sterling, K.M., Jr. (2004). How do glucocorticoids compare to oligo decoys as inhibitors of collagen synthesis and potential toxicity of these therapeutics? J. Cell. Biochem. *92*, 6–15. https://doi.org/10.1002/jcb.20030.

24. Schafer-Korting, M., Kleuser, B., Ahmed, M., Holtje, H.-D., and Korting, H.C. (2005). Glucocorticoids for human skin: new aspects of the mechanism of action. Skin Pharmacol. Physiol. *18*, 103–114. https://doi.org/10.1159/000084907.

25. Ozbakir, B., Crielaard, B.J., Metselaar, J.M., Storm, G., and Lammers, T. (2014). Liposomal corticosteroids for the treatment of inflammatory disorders and cancer. J. Control. Release *190*, 624–636. https://doi.org/10.1016/j.jconrel.2014.05.039.

26. Granot, D., Addadi, Y., Kalchenko, V., Harmelin, A., Kunz-Schughart, L.A., and Neeman, M. (2007). In vivo imaging of the systemic recruitment of fibroblasts to the angiogenic rim of ovarian carcinoma tumors. Cancer Res. *67*, 9180–9189. https://doi.org/10.1158/0008-5472.CAN-07-0684.

27. Ehling, J., Theek, B., Gremse, F., Baetke, S., Möckel, D., Maynard, J., Ricketts, S.-A., Grüll, H., Neeman, M., Knuechel, R., et al. (2014). Micro-CT imaging of tumor angiogenesis: quantitative measures describing micromorphology and vascularization. Am. J. Pathol. *184*, 431–441. https://doi.org/10.1016/j.ajpath.2013.10.014.

28. May, J.-N., Moss, J.I., Mueller, F., Golombek, S.K., Biancacci, I., Rizzo, L., Elshafei, A.S., Gremse, F., Pola, R., Pechar, M., et al. (2024). Histopathological biomarkers for predicting the tumour accumulation of nanomedicines. Nat. Biomed. Eng. *8*, 1366–1378. https://doi.org/10.1038/s41551-024-01197-4.

29. Metselaar, J., Lammers, T., Boquoi, A., Fenk, R., Testaquadra, F., Schemionek, M., Kiessling, F., Isfort, S., Wilop, S., and Crysandt, M. (2023). A phase I first-in-man study to investigate the pharmacokinetics and safety of liposomal dexamethasone in patients with progressive multiple myeloma. Drug Deliv. Transl. Res. *13*, 915–923. https://doi.org/10.1007/s13346-022-01268-6.

30. Deshantri, A.K., Fens, M.H., Ruiter, R.W.J., Metselaar, J.M., Storm, G., van Bloois, L., Varela-Moreira, A., Mandhane, S.N., Mutis, T., Martens, A.C.M., et al. (2019). Liposomal dexamethasone inhibits tumor growth in an advanced human-mouse hybrid model of multiple myeloma. J. Control. Release *296*, 232–240. https://doi.org/10.1016/j.jconrel.2019.01.028.

31. Kroon, J., Buijs, J.T., van der Horst, G., Cheung, H., van der Mark, M., van Bloois, L., Rizzo, L.Y., Lammers, T., Pelger, R.C., Storm, G., et al. (2015). Liposomal delivery of dexamethasone attenuates prostate cancer bone metastatic tumor growth in vivo. Prostate *75*, 815–824. https://doi.org/10.1002/pros.22963.

32. Lammers, T., Sofias, A.M., van der Meel, R., Schiffelers, R., Storm, G., Tacke, F., Koschmieder, S., Brümmendorf, T.H., Kiessling, F., and Metselaar, J.M. (2020). Dexamethasone nanomedicines for COVID-19. Nat. Nanotechnol. *15*, 622–624. https://doi.org/10.1038/s41565-020-0752-z.

33. Banciu, M., Schiffelers, R.M., Metselaar, J.M., and Storm, G. (2008). Utility of targeted glucocorticoids in cancer therapy. J. Liposome Res. *18*, 47–57. https://doi.org/10.1080/08982100801893978.

34. Banciu, M., Metselaar, J.M., Schiffelers, R.M., and Storm, G. (2008). Liposomal glucocorticoids as tumor-targeted anti-angiogenic nanomedicine in B16 melanoma-bearing mice. J. Steroid Biochem. Mol. Biol. *111*, 101–110. https://doi.org/10.1016/j.jsbmb.2008.05.004.

35. Gauthier, A., Fisch, A., Seuwen, K., Baumgarten, B., Ruffner, H., Aebi, A., Rausch, M., Kiessling, F., Bartneck, M., Weiskirchen, R., et al. (2018). Glucocorticoid-loaded liposomes induce a pro-resolution phenotype in human primary macrophages to support chronic wound healing. Biomaterials *178*, 481–495. https://doi.org/10.1016/j.biomaterials.2018.04.006.

36. Anderson, R., Franch, A., Castell, M., Perez-Cano, F.J., Bräuer, R., Pohlers, D., Gajda, M., Siskos, A.P., Katsila, T., Tamvakopoulos, C., et al. (2010). Liposomal encapsulation enhances and prolongs the anti-inflammatory effects of water-soluble dexamethasone phosphate in experimental adjuvant arthritis. Arthritis Res. Ther. *12*, R147. https://doi.org/10.1186/ar3089.

37. Sang, X., Wang, Y., Xue, Z., Qi, D., Fan, G., Tian, F., Zhu, Y., and Yang, J. (2021). Macrophage-targeted lung delivery of dexamethasone improves pulmonary fibrosis therapy via regulating the immune microenvironment. Front. Immunol. *12*, 613907. https://doi.org/10.3389/fimmu.2021.613907.

38. Kwon, J.W., Quan, H., Song, J., Chung, H., Jung, D., Hong, J.J., Na, Y.R., and Seok, S.H. (2022). Liposomal dexamethasone reduces A/H1N1 influenza-associated morbidity in mice. Front. Microbiol. *13*, 845795. https://doi.org/10.3389/fmicb.2022.845795.

39. Gratchev, A. (2017). TGF-β signalling in tumour associated macrophages. Immunobiology *222*, 75–81. https://doi.org/10.1016/j.imbio.2015.11.016.

40. Patel, N.K., Nunez, J.H., Sorkin, M., Marini, S., Pagani, C.A., Strong, A.L., Hwang, C.D., Li, S., Padmanabhan, K.R., Kumar, R., et al. (2022). Macrophage TGF-β signaling is critical for wound healing with heterotopic

ossification after trauma. JCI Insight *7*, e144925. https://doi.org/10.1172/jci.insight.144925.

41. Kunjachan, S., Gremse, F., Theek, B., Koczera, P., Pola, R., Pechar, M., Etrych, T., Ulbrich, K., Storm, G., Kiessling, F., et al. (2013). Noninvasive optical imaging of nanomedicine biodistribution. ACS Nano *7*, 252–262. https://doi.org/10.1021/nn303955n.
42. Quan, L., Zhang, Y., Crielaard, B.J., Dusad, A., Lele, S.M., Rijcken, C.J.F., Metselaar, J.M., Kostková, H., Etrych, T., Ulbrich, K., et al. (2014). Nanomedicines for inflammatory arthritis: head-to-head comparison of glucocorticoid-containing polymers, micelles, and liposomes. ACS Nano *8*, 458–466. https://doi.org/10.1021/nn4048205.
43. Metselaar, J.M., Middelink, L.M., Wortel, C.H., Bos, R., van Laar, J.M., Vonkeman, H.E., Westhovens, R., Lammers, T., Yao, S.-L., Kothekar, M., et al. (2022). Intravenous pegylated liposomal prednisolone outperforms intramuscular methylprednisolone in treating rheumatoid arthritis flares: A randomized controlled clinical trial. J. Control. Release *341*, 548–554. https://doi.org/10.1016/j.jconrel.2021.12.007.
44. Moreau, P., Masszi, T., Grzasko, N., Bahlis, N.J., Hansson, M., Pour, L., Sandhu, I., Ganly, P., Baker, B.W., Jackson, S.R., et al. (2016). Oral Ixazomib, Lenalidomide, and Dexamethasone for Multiple Myeloma. N. Engl. J. Med. *374*, 1621–1634. https://doi.org/10.1056/NEJMoa1516282.
45. Palumbo, A., Chanan-Khan, A., Weisel, K., Nooka, A.K., Masszi, T., Beksac, M., Spicka, I., Hungria, V., Munder, M., Mateos, M.V., et al. (2016). Daratumumab, bortezomib, and dexamethasone for multiple myeloma. N. Engl. J. Med. *375*, 754–766. https://doi.org/10.1056/NEJMoa1606038.
46. Huang, Y., Stylianopoulos, T., Duda, D.G., Fukumura, D., and Jain, R.K. (2013). Benefits of vascular normalization are dose and time dependent–letter. Cancer Res. *73*, 7144–7146. https://doi.org/10.1158/0008-5472.CAN-13-1989.
47. Tolaney, S.M., Boucher, Y., Duda, D.G., Martin, J.D., Seano, G., Ancukiewicz, M., Barry, W.T., Goel, S., Lahdenrata, J., Isakoff, S.J., et al. (2015). Role of vascular density and normalization in response to neoadjuvant bevacizumab and chemotherapy in breast cancer patients. Proc. Natl. Acad. Sci. USA *112*, 14325–14330. https://doi.org/10.1073/pnas.1518808112.
48. Van der Veldt, A.A.M., Lubberink, M., Bahce, I., Walraven, M., de Boer, M.P., Greuter, H.N.J.M., Hendrikse, N.H., Eriksson, J., Windhorst, A.D., Postmus, P.E., et al. (2012). Rapid decrease in delivery of chemotherapy to tumors after anti-VEGF therapy: implications for scheduling of anti-angiogenic drugs. Cancer Cell *21*, 82–91. https://doi.org/10.1016/j.ccr.2011.11.023.
49. Kabbinavar, F., Hurwitz, H.I., Fehrenbacher, L., Meropol, N.J., Novotny, W.F., Lieberman, G., Griffing, S., and Bergsland, E. (2003). Phase II, randomized trial comparing bevacizumab plus fluorouracil (FU)/leucovorin (LV) with FU/LV alone in patients with metastatic colorectal cancer. J. Clin. Oncol. *21*, 60–65. https://doi.org/10.1200/JCO.2003.10.066.
50. Heiss, J.D., Papavassiliou, E., Merrill, M.J., Nieman, L., Knightly, J.J., Walbridge, S., Edwards, N.A., and Oldfield, E.H. (1996). Mechanism of dexamethasone suppression of brain tumor-associated vascular permeability in rats. Involvement of the glucocorticoid receptor and vascular permeability factor. J. Clin. Invest. *98*, 1400–1408. https://doi.org/10.1172/JCI118927.
51. Neuwelt, E.A., Barnett, P.A., Bigner, D.D., and Frenkel, E.P. (1982). Effects of adrenal cortical steroids and osmotic blood-brain barrier opening on methotrexate delivery to gliomas in the rodent: the factor of the blood-brain barrier. Proc. Natl. Acad. Sci. USA *79*, 4420–4423. https://doi.org/10.1073/pnas.79.14.4420.
52. van der Veldt, A.A.M., Lubberink, M., Greuter, H.N., Comans, E.F.I., Herder, G.J.M., Yaqub, M., Schuit, R.C., van Lingen, A., Rizvi, S.N., Mooijer, M.P.J., et al. (2011). Absolute quantification of [(11)C]docetaxel kinetics in lung cancer patients using positron emission tomography. Clin. Cancer Res. *17*, 4814–4824. https://doi.org/10.1158/1078-0432.CCR-10-2933.
53. Lampi, M.C., and Reinhart-King, C.A. (2018). Targeting extracellular matrix stiffness to attenuate disease: from molecular mechanisms to clinical trials. Sci. Transl. Med. *10*, eaao0475. https://doi.org/10.1126/scitranslmed.aao0475.
54. Theek, B., Baues, M., Gremse, F., Pola, R., Pechar, M., Negwer, I., Koynov, K., Weber, B., Barz, M., Jahnen-Dechent, W., et al. (2018). Histidine-rich glycoprotein-induced vascular normalization improves EPR-mediated drug targeting to and into tumors. J. Control. Release *282*, 25–34. https://doi.org/10.1016/j.jconrel.2018.05.002.
55. Gremse, F., Stärk, M., Ehling, J., Menzel, J.R., Lammers, T., and Kiessling, F. (2016). Imalytics preclinical: interactive analysis of biomedical volume data. Theranostics *6*, 328–341. https://doi.org/10.7150/thno.13624.
56. Meurer, S.K., Tezcan, O., Lammers, T., and Weiskirchen, R. (2020). Differential regulation of lipocalin 2 (LCN2) in doxorubicin-resistant 4T1 triple negative breast cancer cells. Cell. Signal. *74*, 109731. https://doi.org/10.1016/j.cellsig.2020.109731.
57. Chen, X., Nadiarynkh, O., Plotnikov, S., and Campagnola, P.J. (2012). Second harmonic generation microscopy for quantitative analysis of collagen fibrillar structure. Nat. Protoc. *7*, 654–669. https://doi.org/10.1038/nprot.2012.009.
58. Korsunsky, I., Fan, J., Slowikowski, K., Zhang, F., Wei, K., Baglaenko, Y., Brenner, M., Loh, P.-R., and Raychaudhuri, S. (2018). Fast, sensitive, and accurate integration of single cell data with Harmony. Preprint at bioRxiv. https://doi.org/10.1101/461954.
59. Harris, M.A., Clark, J., Ireland, A., Lomax, J., Ashburner, M., Foulger, R., Eilbeck, K., Lewis, S., Marshall, B., Mungall, C., et al. (2004). The Gene Ontology (GO) database and informatics resource. Nucleic Acids Res. *32*, D258–D261. https://doi.org/10.1093/nar/gkh036.